# Chapter 9
# Coherent Hemodynamics Spectroscopy: A New Technique to Characterize the Dynamics of Blood Perfusion and Oxygenation in Tissue


**Sergio Fantini, Kristen T. Tgavalekos, Xuan Zang and Angelo Sassaroli**

**Abstract** Hemodynamic-based neuroimaging techniques such as near-infrared spectroscopy (NIRS) and functional magnetic resonance imaging (fMRI) are directly sensitive to the blood volume fraction and oxygen saturation of blood in the probed tissue. The ability to translate such hemodynamic and oxygenation measurements into physiological quantities is critically important to enhance the effectiveness of NIRS and fMRI in a broad range of applications aimed at medical diagnostic or functional assessment. Coherent hemodynamics spectroscopy (CHS) is a novel technique based on the measurement (with techniques such as NIRS or fMRI) and quantitative analysis (with a novel mathematical model) of coherent hemodynamics in living tissues. Methods to induce coherent hemodynamics in humans include controlled perturbations to the mean arterial pressure by paced breathing or by timed inflations of pneumatic cuffs wrapped around the subject's legs. A mathematical model recently outlined translates coherent hemodynamics into physiological measures of the capillary and venous blood transit times, cerebral autoregulation, and cerebral blood flow. A typical method to analyze the optical signal from non-invasive NIRS measurements of the human brain is the modified Beer-Lambert law (mBLL), which does not allow the discrimination of hemodynamics taking place in the scalp and skull from those occurring in the brain cortex. A hybrid method using continuous wave NIRS (with the mBLL) together with frequency-domain NIRS (with a two-layer diffusion model) was successfully used to discriminate oscillatory hemodynamics in the superficial (extracerebral) tissue layer from that in deeper, cerebral tissue.

S. Fantini (✉) · K. T. Tgavalekos · X. Zang · A. Sassaroli
Department of Biomedical Engineering, Tufts University, 4 Colby Street, Medford, MA 02155, USA
e-mail: sergio.fantini@tufts.edu

© Springer Nature Switzerland AG 2018

P. A. Ribeiro and M. Raposo (eds.), *Optics, Photonics and Laser Technology*, Springer Series in Optical Sciences 218, https://doi.org/10.1007/978-3-319-98548-0_9

## 9.1 Hemodynamic-Based Neuroimaging Techniques

With a few exceptions (for example evoked potential tests), functional neuroimaging techniques do not directly measure neural activation; they are sensitive to hemodynamic and metabolic changes associated with brain activity. For example near infrared spectroscopy (NIRS) and functional magnetic resonance imaging (fMRI) are two of the prominent hemodynamic-based neuroimaging techniques. The first one measures the concentrations of oxy- and deoxy-hemoglobin in brain tissue, whereas the latter measures a blood oxygenation level dependent (BOLD) signal that is mostly associated with the concentration of deoxy-hemoglobin in brain tissue and with cerebral blood volume. To assess brain function with these neuroimaging techniques, one needs to characterize the relationship between neural activation and hemodynamic responses, as well as how these hemodynamic responses translate into the measured signals. Noteworthy hemodynamic models proposed in the literature to address these questions include the oxygen diffusion limitation model [1] and a windkessel model [2]. The former model was proposed to account for the large imbalance, observed with positron emission tomography (PET), between blood flow and oxygen consumption changes associated with brain activation. The latter model was introduced to specify the relationship between the dynamics of blood flow and blood volume. These general models were pioneering contributions whose approaches can be adapted to any hemodynamic-based neuroimaging techniques.

Near-infrared spectroscopy (NIRS) is a non-invasive optical method that operates in the 600-900 nm wavelength diagnostic spectral window range. In this wavelength range, oxy-hemoglobin and deoxy-hemoglobin are the main absorbers in tissue, together with some absorption contributions from water and lipids. NIRS has found a variety of applications to the brain, both for functional studies [3–5] and for clinical feasibility [6] in areas such as anesthesiology [7], neurological critical care [8, 9], and electroconvulsive therapy [10]. The spatial and temporal correlations between the BOLD fMRI and the optical NIRS signals elicited by brain activation have been demonstrated in a number of studies [11–14]. Several hemodynamic models have been proposed in the NIRS field, most of them requiring the solution of complex systems of differential equations with many unknown parameters [15–18]. We have recently developed a mathematical model to relate the tissue concentration and saturation of hemoglobin, as measured with NIRS and fMRI, to blood flow, blood volume, and oxidative metabolism [19, 20]. This mathematical model is analytical, and therefore relatively simple and computationally inexpensive.

Recently, we have introduced a novel technique, coherent hemodynamics spectroscopy (CHS), for quantitative studies of tissue hemodynamics based on data collected with NIRS or fMRI [19]. The CHS technique is based on the application of our mathematical model to measured coherent hemodynamics, which may be occurring spontaneously or may be induced by controlled systemic perturbations to the mean arterial blood pressure. In Sect. 9.2, we describe the basic ideas and the general formulation of our mathematical hemodynamic model and of the new CHS technique.

In NIRS, the relative dynamics of oxy- and deoxy-hemoglobin concentrations are usually obtained from the intensity signals measured at a minimum of two wavelengths by applying the modified Beer-Lambert law (mBLL) [21, 22]. Unlike diffusion theory, the mBLL, which has also been used to investigate photon migration in tissues, does not require highly scattering conditions. Nevertheless, the mBLL is fundamented on two key assumptions: (1) the changes in optical intensity are only due to tissue absorption changes; (2) the absorption changes are uniformly distributed within tissue. While the first assumption is often fulfilled to a good approximation, the second one is more questionable and may be violated in a number of cases. For example, brain activation elicited in a number of functional protocols is spatially localized, and so are the associated hemodynamic changes measured with NIRS. Hence, it would be relevant to release the homogeneous absorption changes assumption and instead use a light propagation model that considers (at least partially) the human head complex geometry and the heterogeneous hemodynamics associated with in vivo brain perfusion.

In addition to the physiological heterogeneity intrinsic of living tissue, there is also an issue of anatomical heterogeneity, which is particularly critical in the case of non-invasive NIRS measurements that aim to sense brain tissue with an optical probe placed on the scalp surface. To a first approximation, the human head may be represented by a set of tissue layers such as scalp, skull, subarachnoid space, brain cortex, etc. In the literature, a two-layered diffusion model has been used for measuring the baseline optical properties of two effective tissue layers, the first one representing the scalp and skull (the extracerebral tissue), and the second one representing the brain [23–25]. Short source-detector separations (~0.5 cm) can be introduced in NIRS to provide a reference signal that is representative of the superficial hemodynamics in the scalp and skull, and that is used to regress out superficial-tissue contributions from the optical signal measured at longer (~3 cm) source-detector separations [26–29]. Here, we apply a two-layer diffusion model to multi-distance, frequency-domain NIRS data to estimate the baseline optical properties of extra-cerebral and cerebral tissue layers, as well as the thickness of the extra-cerebral layer. Then, we use phasor analysis, in conjunction with an estimate of the mean partial optical pathlength in the two layers, to assess the induced oscillatory hemodynamics (frequency: 0.059 Hz in this work) in the extra-cerebral and cerebral tissues from continuous wave NIRS measurements at short (8 mm) and long (38 mm) source-detector separations. The two-layer diffusion model and our approach to two-layer hemodynamics assessment are outlined in Sect. 9.3, experimental methods are described in Sect. 9.4, and representative results on a human subject are reported in Sect. 9.5.

## 9.2 Coherent Hemodynamics Spectroscopy for the Quantitative Assessment of Cerebral Hemodynamics

### *9.2.1 Notation for the Tissue Concentrations of Oxy- and Deoxy-Hemoglobin*

As we have seen above, NIRS and fMRI are mostly sensitive to the concentration and oxygen saturation of hemoglobin in blood-perfused tissues. Therefore, to quantitatively describe the tissue hemodynamics as measured by NIRS and fMRI, one needs to consider the temporal evolution of the concentrations of oxy-hemoglobin and deoxy-hemoglobin in tissue. The standard notation for oxy- and deoxy-hemoglobin concentrations is, respectively, [$HbO_2$] and [Hb], or [$O_2Hb$] and [HHb], but we will use here a single-letter notation of $O$ and $D$. Dynamic changes in $O$ and $D$ are considered in the time domain and in the frequency domain. In the time domain, the temporal evolution of changes from baseline or steady-state values ($O_0$ and $D_0$) are indicated as $\Delta O(t)$ and $\Delta D(t)$. In the frequency domain, sinusoidal changes at any frequency $\omega$ are indicated with bold-face phasor notation, $\mathbf{O}(\omega)$ and $\mathbf{D}(\omega)$, where these phasors are two-dimensional vectors whose amplitude and phase represent the amplitude and phase of the corresponding sinusoidal oscillations [30]. Representative time traces of $\Delta O(t)$ and $\Delta D(t)$ are reported in a general case of arbitrary temporal dynamics in Fig. 9.1a, and in a case of quasi sinusoidal oscillations in Fig. 9.1b. The inset of Fig. 9.1b shows the phasor representation of the oscillatory hemodynamics of oxy- and deoxy-hemoglobin concentrations.

Because hemoglobin concentration dynamics are driven by perturbations in three physiological quantities, namely blood volume, blood flow, and metabolic rate of oxygen, we introduce subscripts $V$, $F$, and $\dot{O}$ to indicate the contributions to $O$ and $D$ dynamics from these three physiological sources, respectively. A lack of subscript indicates the overall hemoglobin concentration dynamics resulting from all physiological sources.

We introduce a symbol $S_V$ for the average oxygen saturation of the hemoglobin in the vascular compartment(s) whose volume fraction features dynamic changes. $S_V$ is defined as follows:

$$S_V = \frac{\Delta O_V(t)}{\Delta O_V(t) + \Delta D_V(t)}, \tag{9.1}$$

where $S_V$ is considered to be a constant under the assumption that the volume-varying vascular compartment has a well-defined and constant average saturation, at least over time scales of typical observation times.

It has been previously shown that techniques that are solely sensitive to the tissue concentrations of oxy- and deoxy-hemoglobin (such as NIRS and fMRI) are unable to discriminate the contributions of blood flow and metabolic rate of oxygen to the dynamic changes in $O$ and $D$ [20]. Therefore, we consolidate dynamic changes

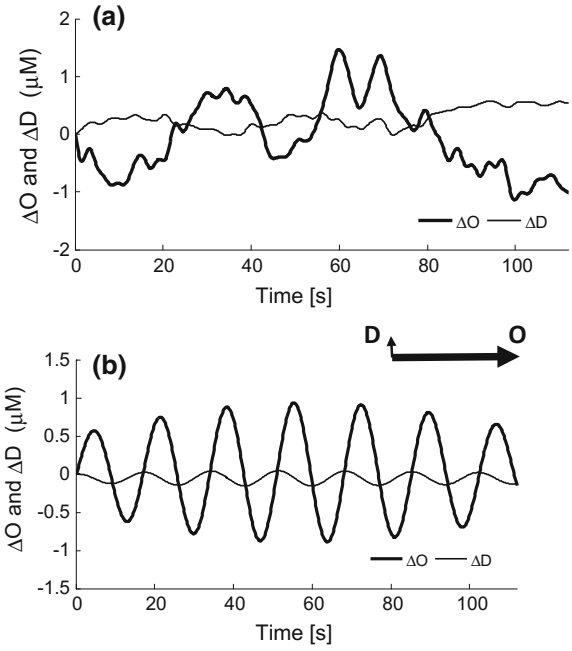


**Fig. 9.1** Representative time traces of dynamic changes in oxy-hemoglobin and deoxy-hemoglobin concentrations ($\Delta O(t)$ and $\Delta D(t)$). **a** Arbitrary dynamics, **b** oscillatory dynamics at a well-defined frequency. The inset of panel (**b**) shows the phasor representation of the quasi sinusoidal oscillations of oxy- and deoxy-hemoglobin concentrations (**O** and **D**)

due to blood flow and metabolic rate of oxygen according to the following notation: $\Delta O_{F,\dot{O}}(t)$ and $\Delta D_{F,\dot{O}}(t)$ in the time domain, $\mathbf{O}_{F,\dot{O}}(\omega)$ and $\mathbf{D}_{F,\dot{O}}(\omega)$ in the frequency domain.

We also introduce notation for the physiological dynamics associated with cerebral blood volume (CBV), cerebral blood flow (CBF), and cerebral metabolic rate of oxygen ($CMRO_2$). We use lower-case notation to indicate the dimensionless, relative dynamics with respect to baseline values (in the time domain) or average values (in the frequency domain), which are indicated with a 0 subscript. Explicitly, $\mathrm{cbv}(t) = (\mathrm{CBV}(t) - \mathrm{CBV}_0)/\mathrm{CBV}_0$, $\mathrm{cbf}(t) = (\mathrm{CBF}(t) - \mathrm{CBF}_0)/\mathrm{CBF}_0$, $\mathrm{cmro}_2(t) = \left(\mathrm{CMRO}_2(t) - \mathrm{CMRO}_{2|0}\right)/\mathrm{CMRO}_{2|0}$ in the time domain, and $\mathbf{cbv}(\omega) = \mathbf{CBV}(\omega)/\mathrm{CBV}_0$, $\mathbf{cbf}(\omega) = \mathbf{CBF}(\omega)/\mathrm{CBF}_0$, $\mathbf{cmro}_2(\omega) = \mathbf{CMRO}_2(\omega)/\mathrm{CMRO}_{2|0}$, in the frequency domain.

### *9.2.2 Time Domain Representation*

According to the notation introduced in Sect. 9.2.1, we can write:

$$\Delta O(t) = \Delta O_V(t) + \Delta O_{F,\dot{O}}(t), \tag{9.2}$$

$$\Delta D(t) = \Delta D_V(t) + \Delta D_{F,\dot{O}}(t), \tag{9.3}$$

and from (9.1) it immediately follows that:

$$(1 - S_V)\Delta O_V(t) = S_V \Delta D_V(t). \tag{9.4}$$

Equation (9.4) states that the volume-driven changes $\Delta O_V(t)$ and $\Delta D_V(t)$ are synchronous and proportional to each other, with a constant of proportionality that is determined by the average oxygen saturation of the volume-varying vascular compartment(s).

Because blood flow and metabolic rate of oxygen dynamics solely affect the rate of oxygen removal from hemoglobin, which in turn transform oxy-hemoglobin into deoxy-hemoglobin, it follows that:

$$\Delta O_{F,\dot{O}}(t) = -\Delta D_{F,\dot{O}}(t). \tag{9.5}$$

Equation (9.5) states that the dynamic changes $\Delta O_{F,\dot{O}}(t)$ and $\Delta D_{F,\dot{O}}(t)$ resulting from blood flow and metabolic rate of oxygen changes are also proportional to each other, with a proportionality factor of $-1$.

Equations (9.2)–(9.5) provide relationships between the overall oxy- and deoxy-hemoglobin concentration dynamics ($\Delta O(t)$, $\Delta D(t)$) and their components due to blood volume changes ($\Delta O_V(t)$, $\Delta D_V(t)$) or to blood flow and metabolic rate of oxygen changes $\left(\Delta O_{F,\dot{O}}(t), \Delta D_{F,\dot{O}}(t)\right)$. In order to translate dynamic measurements of hemoglobin concentration into measurements of the underlying changes in blood volume cbv($t$)), blood flow (cbf($t$)), and metabolic rate of oxygen (cmro$_2$($t$)), one needs to specify the relationship between hemoglobin concentration and physiological quantities. This critical point is addressed in Sect. 9.2.4.1.

### *9.2.3 Frequency Domain Representation*

The time-domain representation provided by (9.2)–(9.5) is expressed by the following phasor equations in the frequency domain:

$$\mathbf{O}(\omega) = \mathbf{O}_V(\omega) + \mathbf{O}_{F,\dot{O}}(\omega), \tag{9.6}$$

$$\mathbf{D}(\omega) = \mathbf{D}_V(\omega) + \mathbf{D}_{F,\dot{O}}(\omega), \tag{9.7}$$

$$(1 - S_V)\mathbf{O}_V(\omega) = S_V \mathbf{D}_V(\omega). \tag{9.8}$$

$$\mathbf{O}_{F,\dot{O}}(\omega) = -\mathbf{D}_{F,\dot{O}}(\omega). \tag{9.9}$$

Equation (9.8) states that the volume-driven oscillations $\mathbf{O}_V(\omega)$ and $\mathbf{D}_V(\omega)$ are in phase and their relative amplitude can be determined by the average oxygen saturation of the volume-oscillating vascular compartment(s). Equation (9.9) states that the dynamic oscillations $\mathbf{O}_{F,\dot{O}}(\omega)$ and $\mathbf{D}_{F,\dot{O}}(\omega)$ resulting from blood flow and metabolic rate of oxygen oscillations are in opposition of phase and have the same amplitude.

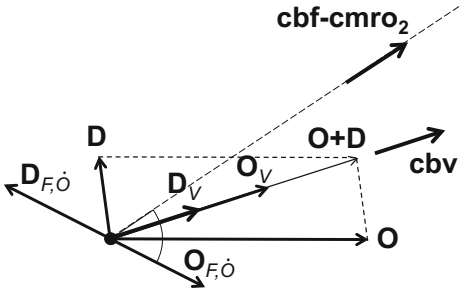


**Fig. 9.2** Phasor decomposition of measured oscillations of oxy-hemoglobin (**O**) and deoxy-hemoglobin (**D**) concentrations, into their components due to blood volume ($\mathbf{O}_V$ and $\mathbf{D}_V$) and the combination of blood flow and oxygen consumption ($\mathbf{O}_{F,\dot{O}}$ and $\mathbf{D}_{F,\dot{O}}$) oscillations. The cerebral blood volume phasor (**cbv**) is in phase with $\mathbf{O}_V$, whereas the blood flow and metabolic rate of oxygen phasor (**cbf** $-$ **cmro**$_2$) leads $\mathbf{O}_{F,\dot{O}}$ by the angle indicated in the figure (as described in Sect. 9.2.4.2)

We highlight the elegance of the phasor representation of (9.6)–(9.9) by illustrating how these equations can be solved graphically. The system of (9.6)–(9.9) is a set of four phasor equations, i.e. four 2-D vector equations, which correspond to eight scalar equations. Considering that $\mathbf{O}(\omega)$ and $\mathbf{D}(\omega)$ are measurable quantities (certainly both of them with NIRS), this set of equations contains nine unknowns: the two phasor components of each of $\mathbf{O}_V$, $\mathbf{O}_{F,\dot{O}}$, $\mathbf{D}_V$, and $\mathbf{D}_{F,\dot{O}}$, and the scalar quantity $S_V$. Therefore, the number of unknowns exceeds the number of equations by one [31]. To solve this system of equations one may assume a value for $S_V$, which has an upper limit given by the arterial saturation (say, 1) and a lower limit given by the lowest venous saturation (say, 0.5 under normal conditions at rest, but possibly lower under special conditions). In Fig. 9.2, we illustrate how to solve the system of (9.6)–(9.9) under the assumption that $S_V = 0.65$. The measured phasors **O** and **D** are combined by phasor addition into $\mathbf{O} + \mathbf{D}$, which represents the phasor of total hemoglobin concentration. Because of (9.9), only $\mathbf{O}_V$ and $\mathbf{D}_V$ contribute to the total hemoglobin concentration phasor (since $\mathbf{O}_{F,\dot{O}} + \mathbf{D}_{F,\dot{O}} = 0$), and (9.8) specifies that $\mathbf{O}_V$ and $\mathbf{D}_V$ are in phase with each other and therefore with $\mathbf{O} + \mathbf{D}$. As a result, $\mathbf{O}_V$ and $\mathbf{D}_V$ are aligned with $\mathbf{O} + \mathbf{D}$ and the magnitude of $\mathbf{O}_V$ is $S_V$ (or 0.65) times the magnitude of $\mathbf{O} + \mathbf{D}$ whereas $\mathbf{D}_V$ is $1 - S_V$ (or 0.35) times $\mathbf{O} + \mathbf{D}$. From (9.6) and (9.7) it follows that $\mathbf{O}_{F,\dot{O}}$ is the vector from the tip of $\mathbf{O}_V$ to the tip of **O**, and $\mathbf{D}_{F,\dot{O}}$ is the vector from the tip of $\mathbf{D}_V$ to the tip of **D**. $\mathbf{O}_{F,\dot{O}}$ and $\mathbf{D}_{F,\dot{O}}$ are translated to start at the origin in Fig. 9.2, to show that they are opposite to each other, as per (9.9).

Figure 9.2 shows how, from the measured phasors (i.e. oscillations) of oxy- and deoxy-hemoglobin concentrations, one can find the phasor component associated with blood volume oscillations, and the phasor component associated with blood flow and metabolic rate of oxygen oscillations. Now, similar to the time-domain case, the key missing piece to translate oscillations of hemoglobin concentration into oscillations of physiological quantities is knowledge of the relationships between

$\mathbf{O}_V(\omega)$ and $\mathbf{cbv}(\omega)$, and between $\mathbf{O}_{F,\dot{O}}(\omega)$ and $\mathbf{cbf}(\omega)$, $\mathbf{cmro}_2(\omega)$. This critical point is addressed in Sect. 9.2.4.2.

### *9.2.4 A Hemodynamic Model to Relate Hemoglobin Concentrations to Physiological Quantities*

A mathematical model has been recently developed to derive analytical relationships between the concentrations of oxy- and deoxy-hemoglobin concentrations in tissue, and the key physiological quantities (blood volume, blood flow, and metabolic rate of oxygen) that determine the steady-state values and drive dynamic changes in the concentrations of oxy- and deoxy-hemoglobin in living tissue [19, 20]. This model relies on the fact that every red blood cell, and the hemoglobin molecules it contains, must travel from an arterial compartment (which delivers blood to tissue), through a capillary compartment (including small arterioles, where oxygen exchange from blood to tissue occurs), to a venous compartment (which drains blood from tissue). Because oxygen diffusion from blood to tissue only occurs at the capillary level (here we include in the capillary compartment the smaller arterioles that are also involved with oxygen diffusion), the model treats the oxygen desaturation of blood according to just two parameters: the mean capillary transit time ($t^{(c)}$) and the rate constant of oxygen diffusion from capillary blood to tissue ($\alpha$). Dynamic perturbations to either parameter (changes in blood flow velocity for $t^{(c)}$, changes in metabolic rate of oxygen for $\alpha$) cause dynamic perturbations to the oxygen saturation of capillary blood, which propagate to the venous compartment according to another key model parameter, the venous blood transit time ($t^{(v)}$). We observe that while $t^{(c)}$ is a well-defined parameter, independent of the tissue volume sampled (as long as it includes the entire capillary compartment, which has linear dimensions of 1 mm or less), $t^{(v)}$ monotonically increases with the volume of probed tissue, because longer and longer venous drainage vessels are included in larger and larger probed volumes.

The model derives the dynamic effects of ideal step changes in blood volume, blood flow velocity, and metabolic rate of oxygen to the tissue concentrations of oxy- and deoxy-hemoglobin, and translates them to general perturbations with transfer function analysis, i.e. by considering the microvasculature as a linear, time-invariant system. In this approach, the microvascular system (for which dynamics in blood volume, blood flow, and metabolic rate of oxygen are the input, and the concentrations of oxy- and deoxy-hemoglobin are the output) is fully described by impulse response functions in the time domain, and by transfer functions in the frequency domain.

Because of the relationships between dynamic changes in oxy- and deoxy-hemoglobin, expressed by (9.2)–(9.5) in the time domain and by (9.6)–(9.9) in the frequency domain, we only need to specify the effects of blood volume, blood flow, and metabolic rate of oxygen on the concentration of one hemoglobin species, say oxy-hemoglobin. This is what we report in Sects. 9.2.4.1 for arbitrary hemodynamics, and in Sect. 9.2.4.2 for oscillatory hemodynamics.

#### 9.2.4.1 Time-Domain Relationships

The contribution of oxy-hemoglobin concentration changes due to blood volume dynamics ($\Delta O_V$) is written as follows [19]:

$$\begin{aligned}\Delta O_V(t) =& \text{ctHb}\Big[S^{(a)}\text{CBV}_0^{(a)}\text{cbv}^{(a)}(t) + \left\langle S^{(c)}\right\rangle \mathcal{F}^{(c)}\text{CBV}_0^{(c)}\text{cbv}^{(c)}(t) \\ &+ S^{(v)}\text{CBV}_0^{(v)}\text{cbv}^{(v)}(t)\Big]\end{aligned} \tag{9.10}$$

being ctHb the blood hemoglobin concentration, $S$ is the oxygen saturation of hemoglobin, $\text{CBV}_0$ is the baseline blood volume, $\text{cbv}(t)$ is the relative blood volume change (with respect to baseline), $\mathcal{F}^{(c)}$ is the Fåhraeus factor (the ratio of capillary to large vessel hematocrit), and superscripts $(a)$, $(c)$, and $(v)$ specify the arterial, capillary, and venous vascular compartments, respectively. Equation (9.10) shows that blood volume dynamics result in instantaneous changes in oxy-hemoglobin concentration, through proportionality factors expressed in terms of the concentration and oxygen saturation of hemoglobin in blood.

The contribution of oxy-hemoglobin concentration changes ($\Delta O_{F,\dot{O}}$) due to blood flow and metabolic rate of oxygen dynamics can be expressed as [19]:

$$\begin{aligned}&\Delta O_{F,\dot{O}}(t) \\ &= \text{ctHb}\left[\frac{\left\langle S^{(c)}\right\rangle}{S^{(v)}}\left(\left\langle S^{(c)}\right\rangle - S^{(v)}\right)\mathcal{F}^{(c)}\text{CBV}_0^{(c)}h_{RC-LP}^{(c)}(t) + \left(S^{(a)} - S^{(v)}\right)\text{CBV}_0^{(v)}h_{G-LP}^{(v)}(t)\right] \\ &\quad * \left(\text{cbf}(t) - \text{cmro}_2(t)\right)\end{aligned} \tag{9.11}$$

The $*$ is here indicating a convolution product, $\text{cbf}(t)$ and $\text{cmro}_2(t)$ are the relative blood flow and metabolic oxygen rate changes (with respect to baseline), and $h_{RC-LP}^{(c)}(t)$ and $h_{G-LP}^{(v)}(t)$ are the impulse response functions that describe the low-pass (LP) effects related to the microcirculation in the capillary and venous vascular compartments, respectively.

The capillary impulse response function is approximated by that of a low-pass resistor-capacitor (RC) circuit equivalent:

$$h_{RC-LP}^{(c)}(t) = u(t)\frac{1}{\tau^{(c)}}e^{-t/\tau^{(c)}}, \tag{9.12}$$

where $u(t)$ is the unit step function (which is 0 for a negative argument, and 1 for a positive or zero argument) and $\tau^{(c)}$ is the capillary time constant ($\tau^{(c)}$) that is related to $t^{(c)}$ as follows:

$$\tau^{(c)} = \frac{t^{(c)}}{e}. \tag{9.13}$$

The venous impulse response function is approximated by that of a time-shifted Gaussian low-pass filter:

$$h^{(v)}_{G-LP}(t) = \frac{1}{t^{(v)}_r} e^{-\pi\left(t-t^{(v)}_{0.5}\right)^2/\left(t^{(v)}_r\right)^2}, \tag{9.14}$$

where $t^{(v)}_{0.5}$ is the time-shift constant and $t^{(v)}_r$ is the time-width constant. These two time constant are close to each other, since $t^{(v)}_{0.5} = (5/6)t^{(v)}_r$. If we identify $t^{(v)}_{0.5}$ with the venous time constant ($\tau^{(v)}$), one finds that $\tau^{(v)}$ is the mean of the capillary and venous blood transit times:

$$\tau^{(v)} = \frac{t^{(c)} + t^{(v)}}{2}. \tag{9.15}$$

This treatment shows that any dynamic changes in blood flow or metabolic rate of oxygen result in delayed and temporally spread changes in the tissue concentrations of oxy- and deoxy-hemoglobin. These temporal effects occur on a time scale that is determined by the capillary and venous blood transit times (as specified by the capillary and venous time constants in (9.13) and (9.15)), and is analytically reflected in the convolution product of (9.11).

#### 9.2.4.2 Frequency-Domain Relationships

The oxy-hemoglobin phasor ($\mathbf{O}_V$) that describes oxy-hemoglobin dynamics due to sinusoidal oscillations of blood volume at angular frequency $\omega$ is written as follows [19]:

$$\begin{aligned}\mathbf{O}_V(\omega) = \mathrm{ctHb}\Big[ & S^{(a)}\mathrm{CBV}^{(a)}_0 \mathbf{cbv}^{(a)}(\omega) + \left\langle S^{(c)}\right\rangle \mathcal{F}^{(c)} \mathbf{cbv}^{(c)}(\omega) \\ & + S^{(v)}\mathrm{CBV}^{(v)}_0 \mathbf{cbv}^{(v)}(\omega)\Big]\end{aligned} \tag{9.16}$$

where $\mathbf{cbv}(\omega)$ is the relative blood volume phasor (normalized to the mean value of blood volume), and we use the same notation as in (9.10). Equation (9.16) shows that blood volume oscillations cause in-phase oscillations of oxy-hemoglobin concentration. In fact, $\mathbf{O}_V$ and the blood volume phasors are linked by a linear relationship with all real and positive coefficients that are expressed in terms of the concentration and oxygen saturation of hemoglobin in blood.

The oxy-hemoglobin phasor ($\mathbf{O}_{F,\dot{O}}$) that describes oxy-hemoglobin dynamics due to sinusoidal oscillations of blood flow and metabolic rate of oxygen is written as follows [19]:

$$\begin{aligned}\mathbf{O}_{F,\dot{O}}(\omega) = \mathrm{ctHb}\Bigg[ & \frac{\left\langle S^{(c)}\right\rangle}{S^{(v)}}\left(\left\langle S^{(c)}\right\rangle - S^{(v)}\right)\mathcal{F}^{(c)}\mathrm{CBV}^{(c)}_0 \mathcal{H}^{(c)}_{RC-LP}(\omega) \\ & + \left(S^{(a)} - S^{(v)}\right)\mathrm{CBV}^{(v)}_0 \mathcal{H}^{(v)}_{G-LP}(\omega)\Bigg][\mathbf{cbf}(\omega) - \mathbf{cmro}_2(\omega)]\end{aligned} \tag{9.17}$$

where $\mathbf{cbf}(\omega)$ and $\mathbf{cmro}_2(\omega)$ are the relative blood flow and metabolic rate of oxygen phasors (normalized to the corresponding mean values), and $\mathcal{H}^{(c)}_{RC-LP}(\omega)$ and $\mathcal{H}^{(v)}_{G-LP}(\omega)$ are the transfer functions that describe the low-pass (LP) effects associated with the microcirculation in the capillary and venous vascular compartments, respectively. Notice that the convolution product in the time domain (9.11) is replaced by a regular product in the frequency domain (9.17).

The capillary and venous transfer functions are given by the Fourier transform of the capillary and venous pulse response functions given in (9.12) and (9.14), respectively:

$$\mathcal{H}^{(c)}_{RC-LP}(\omega) = \frac{1}{1 + i\omega\tau^{(c)}}, \tag{9.18}$$

$$\mathcal{H}^{(v)}_{G-LP}(\omega) = e^{-0.11\left[\omega\tau^{(v)}\right]^2} e^{-i\omega\tau^{(v)}}. \tag{9.19}$$

The low-pass transfer functions of (9.18) and (9.19) have a negative phase of $-\tan^{-1}\left(\omega\tau^{(c)}\right)$ and $-\omega\tau^{(v)}$, respectively. Therefore, (9.17) shows that the phase of $\mathbf{O}_{F,\dot{O}}$ is more negative than that of $\mathbf{cbf} - \mathbf{cmro}_2$; in other words, the oscillations of oxy-hemoglobin concentration trail the driving oscillations of blood flow and metabolic rate of oxygen. This is the reason that the phasor $\mathbf{cbf}(\omega) - \mathbf{cmro}_2(\omega)$ is not aligned (i.e. in phase) with the phasor $\mathbf{O}_{F,\dot{O}}$ in Fig. 9.2, and (9.17) specifies the phase angle (indicated in Fig. 9.2) between these two phasors. This phase lag is the frequency-domain equivalent of the delay between dynamic changes in the tissue concentration of oxy-hemoglobin and the driving changes in CBF or $CMRO_2$ that were observed in the time-domain case in relation to (9.11).

#### 9.2.4.3 Modeling Cerebral Autoregulation

Cerebral autoregulation is the homeostatic regulation of cerebral blood flow that maintains a relatively constant brain perfusion under conditions of variable mean arterial pressure. Because relatively fast blood pressure changes (on a time scale of less than one second) do not typically result in effective autoregulation, whereas slower blood pressure changes are effectively compensated by cerebrovascular resistance changes, autoregulation is often modeled with high-pass filters. Such filters are usually applied to linear systems that consider arterial blood pressure as the input and cerebral blood flow as the output. In cases where continuous arterial blood pressure measurements are not available, we have considered a high-pass filter between cerebral blood volume (the input) and cerebral blood flow (the output). Of course, cerebral blood volume is not necessarily a suitable surrogate for mean arterial pressure. However, blood volume measured by NIRS is mostly representative of the microvasculature, with greater contributions from the more compliant venous compartments, and it was reported that dynamic NIRS measurements of blood volume closely match (except from a slight delay) mean arterial pressure traces [32].

In the time domain, the relationship between blood volume and blood flow is:

$$\mathrm{cbf}(t) = k h^{(\mathrm{AR})}_{RC-HP}(t) * \mathrm{cbv}(t), \tag{9.20}$$

where $k$ is a constant and $h^{(\mathrm{AR})}_{RC-HP}(t)$ is the high-pass (HP) impulse response function, approximated here by the one for a high-pass resistor-capacitor (RC) equivalent electrical circuit:

$$h^{(\mathrm{AR})}_{RC-HP}(t) = \delta(t) - u(t)\frac{1}{\tau^{(\mathrm{AR})}} e^{-t/\tau^{(\mathrm{AR})}}, \tag{9.21}$$

where $u(t)$ is the unit step function and $\tau^{(\mathrm{AR})}$ is the time constant for autoregulation.

The corresponding frequency-domain relationships, expressed in phasor notation and invoking the autoregulation transfer function, given by the Fourier transform of (9.21), are:

$$\mathbf{cbf}(\omega) = k\mathcal{H}^{(\mathrm{AR})}_{RC-HP}(\omega)\mathbf{cbv}(\omega), \tag{9.22}$$

$$\mathcal{H}^{(\mathrm{AR})}_{RC-HP}(\omega) = \frac{i\omega\tau^{(\mathrm{AR})}}{1 + i\omega\tau^{(\mathrm{AR})}}. \tag{9.23}$$

The high-pass transfer function of (9.23) has a positive phase of $\tan^{-1}(1/(\omega\tau^{(c)}))$. Therefore, (9.22) shows that the phase of **cbf** is more positive than that of **cbv**; in other words, CBF oscillations lead CBV oscillations. This is reflected in the time domain by the fact that higher frequencies (corresponding to temporal features having faster time scales) are retained by the high pass filter. Therefore, peak values of dynamic changes are reached at earlier times for $\mathrm{cbf}(t)$ than for $\mathrm{cbv}(t)$.

### *9.2.5 Coherent Hemodynamics Spectroscopy (CHS)*

The above Sects. 9.2.1–9.2.4 provide the conceptual framework for the novel technique of coherent hemodynamics spectroscopy, or CHS [19]. CHS is based on coherent hemodynamics that allow for considering, at least to a first approximation, the microvasculature to behave as a linear time invariant system. The basic assumption is that, over the observation period, there is a high level of coherence between the driving physiological dynamics of blood volume, blood flow, and metabolic rate of oxygen, and the resulting, measurable dynamics of oxy- and deoxy-hemoglobin concentrations in tissue. Under these conditions, the above analytical treatment holds, and one can perform quantitative CHS measurements either in the time domain (considering general temporal dynamics such as those illustrated in Fig. 9.1a) or in the frequency domain (considering oscillatory dynamics such as those illustrated in Fig. 9.1b).

Quantitative CHS allows for the determination of a number of physiological quantities related to tissue perfusion, oxygenation, and hemodynamics that can find significant applications in diagnostic or functional studies of living tissue. For example, we have shown the ability of CHS to measure the cerebral capillary transit time in hemodialysis patients and healthy controls [33], the cutoff frequency for autoregulation in healthy subjects under normal breathing conditions and during hyperventilation-induced hypocapnia [34], and the absolute value and relative dynamics of cerebral blood flow [35].

## 9.3 Hybrid Method Based on Two-Layer Diffusion Theory and the Modified Beer-Lambert Law to Study Cerebral Hemodynamic Oscillations

As discussed in Sect. 9.1, some tissues cannot be assumed to be optically homogeneous when measured with non-invasive NIRS from the tissue surface. In particular, the human head features tissue layers such as the scalp, skull, dura mater and subdural space, arachnoid mater and subarachnoid space, grey matter and white matter. These different tissue types are characterized by different optical properties (i.e. absorption and reduced scattering coefficients) that must be taken into account to accurately describe light propagation from the illumination to the collection points. There is a vast literature related to diffusive layered models that can be classified into theoretical or phantom studies [36–39], and in vivo studies [23–25]. These studies were aimed at measuring either the absolute optical properties of layered tissue-like phantoms or the baseline (i.e. steady state) optical properties of layered biological tissues.

In addition to the study of steady state conditions, it is important to apply two or multi-layered models also for studying small perturbations in the optical properties of heterogeneous tissues such as those associated with cerebral and extra-cerebral hemodynamic changes, either spontaneous or induced. In particular, we could apply diffusive layered models to analyze CHS data and extract the relevant physiological parameters that pertain to the brain. However, due to signal-to-noise considerations, detecting small hemodynamic oscillations using time-resolved methods is challenging. For example, in frequency domain (FD) NIRS, expected perturbations in the absorption coefficient as induced by typical CHS maneuvers, should induce phase changes that are comparable to the noise level. For these reasons, we propose to take advantage of both FD and continuous wave (CW) NIRS measurements in order to measure the oscillations in the concentration of oxy- and deoxy-hemoglobin in brain tissue during typical CHS protocols.

The FD component of our method is based on FD NIRS measurements to estimate the baseline optical properties of the head, which is considered as a two-layer medium, with the first layer comprising extracerebral tissue, and the second layer representing the brain. By using an inversion procedure based on a two-layer diffusion model [25], we are able to derive not only the optical properties of the two layers

but also the thickness of the extracerebral tissue layer. In our previous work, the inversion procedure was tested on both phantoms and human subjects [25]. Knowledge of the optical properties of the two layers and the thickness of the first layer allows for the estimation of the partial mean pathlengths travelled by detected photons in each of the two layers, which are required for disentangling the contributions to the measured signal from hemodynamic oscillations occurring in the extracerebral tissue from those occurring in the brain. In the next two sections we describe in detail the mathematical models of the proposed method of data analysis.

### 9.3.1 *Diffusion Theory for a Two-Layered Cylindrical Medium*

A two-layer diffusive medium is divided into a top region (first layer) and bottom region (second layer). The two media have different optical properties, namely the absorption coefficient ($\mu_a$) and the reduced scattering coefficient ($\mu_s'$). The diffusion equation for an intensity-modulated point source in the frequency domain (FD) is written as:

$$\nabla \cdot [D_0(\mathbf{r})\nabla\phi(\mathbf{r}, \Omega)] - \left[\mu_a(\mathbf{r}) + i\frac{\Omega}{v}\right]\phi(\mathbf{r}, \Omega) = -P_{AC}(\Omega)\delta(\mathbf{r}). \tag{9.24}$$

In (9.24) $\phi$ is the fluence rate, i.e. the optical power per unit area impinging from all directions (units: W/m$^2$) at an arbitrary field point inside the medium (at position vector: $\mathbf{r}$), $D_0 = 1/(3\mu_s')$ is the optical diffusion coefficient, $v$ is the speed of light in the medium, $\Omega$ is the angular modulation frequency of the light intensity (in this study $\Omega/(2\pi)$ is 110 MHz), $\delta$ is the Dirac delta, and $P_{AC}$ is the source power. Here we consider a cylindrical geometry, where one of the circular bases of the cylinder acts as the surface available to the optical probe (light sources and optical detectors), and the physical size of the cylinder (height and diameter) is large enough to neglect any boundary effects at the sides and at the circular base opposite to the one accessible to the optical probe. For a point source incident at the center of the circular base, the general solution of the two-layer diffusion equation in cylindrical coordinates ($\mathbf{r} = (\rho, \theta, z)$; $z$ is the direction of the cylinder's axis pointing inside the medium) is given by [40]:

$$\phi_k(\mathbf{r}, \Omega) = \frac{P_{AC}(\Omega)}{\pi a'^2}\sum_{n=1}^{\infty} G_k(s_n, z, \Omega)J_0(s_n\rho)J_1^{-2}(a's_n) \tag{9.25}$$

where $\phi_k$ is the fluence rate in the $k$th layer of the medium ($k = 1, 2$), $s_n$ are the positive roots of the 0th-order Bessel function of the first kind divided by $a' = a + z_b$, (where $a$ is the radius of the cylinder), and $J_m$ is the Bessel function of the first kind of order $m$. Also, $z_b$ is the distance between the extrapolated and the real boundary, $z_b$

$= 2D_{01}(1+R_{\text{eff}})/(1-R_{\text{eff}})$, $R_{\text{eff}}$ is the fraction of photons that are internally diffusely reflected at the cylinder boundary and $D_{01}$ is the optical diffusion coefficient in the first layer. Here, we report the solution for $G_k$ only for the first layer ($k = 1$), since it is the layer where the reflectance is calculated. For the first layer (the one illuminated by the light source), $G_1$ is given by the following expression:

$$\begin{aligned} G_1(s_n, z, \Omega) = & \frac{\exp(-\alpha_1|z - z_0|) - \exp[\alpha_1(z + z_0 + 2z_b)]}{2D_{01}\alpha_1} \\ & + \frac{\sinh[\alpha_1(z_0 + z_b)]\sinh[\alpha_1(z + z_b)]}{D_{01}\alpha_1 \exp[\alpha_1(L + z_b)]} \\ & \times \frac{D_{01}\alpha_1 - D_{02}\alpha_2}{D_{01}\alpha_1 \cosh[\alpha_1(L + z_b)] + D_{02}\alpha_2 \sinh[\alpha_1(L + z_b)]} \end{aligned} \tag{9.26}$$

where $L$ is the thickness of the first layer, $z_0$ is the mean transport scattering length in the top layer ($1/\mu'_{s1}$), and $\alpha_k$ ($k = 1, 2$) is given by:

$$\alpha_k = \sqrt{\frac{\mu_{ak}}{D_{0k}} + s_n^2 + \frac{i\,\Omega}{D_{0k}v}} \tag{9.27}$$

Equation (9.26) is attained in the limiting case of an infinite second layer in the $z$ direction, and for the situation where the two layers have the same refractive index [40]. In (9.27), $D_{0k}$ and $\mu_{ak}$ are the $k$th layer diffusion and the absorption coefficients. For the calculation of the optical diffuse reflectance ($R$), one may apply Fick's law:

$$R(\rho, \Omega) = D_{01}\frac{\partial}{\partial z}\phi_1(\rho, z, \Omega)\Big|_{z=0} \tag{9.28}$$

From the reflectance expression (as fully described by a complex function), one can determine the amplitude, or AC($\rho$, $\Omega$) and the phase $\theta(\rho, \Omega)$, the two main quantities measured in FD NIRS, as follows: $\text{AC}(\rho, \Omega) = |R(\rho, \Omega)|$, $\theta(\rho, \Omega) = \text{Arg}[R(\rho, \Omega)]$.

The above solution of the diffusion equation was used as the forward solver in an inversion methodology, based on the Levenberg-Marquardt method which allows to recover the two layers optical properties ($\mu_a$, $\mu'_s$) and the first layer thickness from measured AC amplitude and phase data at six source detector separations [25]. When data taken on human subjects are considered, the inversion procedure is run by using average values of AC amplitude and phase data acquired during baseline, allowing us to recover the average baseline oxy- and deoxy-hemoglobin concentrations in extracerebral tissue and in the brain.

### 9.3.2 mBLL for Measuring Hemodynamic Oscillations

CW intensity oscillations due to absorption oscillations in tissue are given (for the case of a two-layered model of tissue) by the phasor equation:

$$\mathbf{i}(d_j, \lambda, \omega) = -\sum_{i=1}^{2} \langle l_i(d_j, \lambda) \rangle \boldsymbol{\mu}_{ai}(\lambda, \omega) \tag{9.29}$$

In (9.29), $\mathbf{i}(d_j, \lambda, \omega)$ is the phasor associated with sinusoidal intensity oscillations normalized to the baseline, or average intensity: $\frac{I(d_j,\lambda,\omega,t)-I_b(d_j,\lambda)}{I_b(d_j,\lambda)}$, where $I(d_j, \lambda, \omega, t)$ and $I_b(d_j, \lambda)$ are the instantaneous and baseline (or average) intensities, respectively, $d_j$ is the source detector separation ($j = 1, \ldots, 6$ in this work), $\lambda$ is the wavelength ($\lambda = 690, 830$ nm in this work) and $i$ is the layer index ($i = 1, 2$). $\langle l_i(d_j, \lambda) \rangle$ is the mean optical pathlength in layer $i$ for photons detected at $d_j$. $\boldsymbol{\mu}_{ai}(\lambda, \omega)$ is the phasor associated with sinusoidal absorption oscillations in layer $i$, normalized to the baseline, or average absorption coefficient: $\frac{\mu_{ai}(\lambda,\omega,t)-\mu_{aib}(\lambda)}{\mu_{aib}(\lambda)}$, where $\mu_{ai}(\lambda, \omega, t)$, and $\mu_{aib}(\lambda)$ are the instantaneous and baseline (or average) absorption coefficients, respectively, in layer $i$. Note that $\mu_{aib}(\lambda)$ is measured by the FD method described in the previous section for both layers $i = 1, 2$. The phasors associated with oxy- and deoxy-hemoglobin oscillations in the two layers (which comprise contributions from both blood volume and blood flow oscillations) are related to the absorption phasors by the relationship:

$$\boldsymbol{\mu}_{ai}(\lambda, \omega) = \varepsilon_{\mathrm{HbO2}}(\lambda)\mathbf{O}_i(\omega) + \varepsilon_{\mathrm{Hb}}(\lambda)\mathbf{D}_i(\omega) \tag{9.30}$$

where $\mathbf{O}_i$ and $\mathbf{D}_i$ are the oxy- and deoxyhemoglobin phasors, respectively, in layer $i$, and $\varepsilon_{\mathrm{HbO2}}$ and $\varepsilon_{\mathrm{Hb}}$ are the wavelength-dependent extinction coefficients of oxy- and deoxy-hemoglobin.

Equation (9.29) represents a generalized mBLL for a two-layered medium, and it can be re-written in the form of the standard mBLL by introducing an effective absorption phasor that depends on the source-detector separation:

$$\mathbf{i}(d_j, \lambda, \omega) = -\langle L(d_j, \lambda) \rangle \boldsymbol{\mu}_{a,\mathrm{eff}}(d_j, \lambda, \omega) \tag{9.31}$$

In (9.31), the intensity phasor is expressed in terms of an effective absorption coefficient phasor $\boldsymbol{\mu}_{a,\mathrm{eff}}(d_j, \lambda, \omega)$ (which depends on $d_j$) and the total mean pathlength, $\langle L(d_j, \lambda) \rangle$, traveled by the photons that are detected at a source-detector distance $d_j$. The effective absorption coefficient phasor is related to effective oxy- and deoxy-hemoglobin concentration phasors by a relationship formally similar to (9.30):

$$\boldsymbol{\mu}_{a,\mathrm{eff}}(d_j, \lambda, \omega) = \varepsilon_{\mathrm{HbO2}}(\lambda)\mathbf{O}_{\mathrm{eff}}(d_j, \omega) + \varepsilon_{\mathrm{Hb}}(\lambda)\mathbf{D}_{\mathrm{eff}}(d_j, \omega) \tag{9.32}$$

By using (9.29)–(9.32), we derive the following system of equations:

$$\mathbf{O}_{\text{eff}}(d_j, \omega) = \alpha_1(d_j)\mathbf{D}_1(\omega) + \alpha_2(d_j)\mathbf{O}_1 + \alpha_3(d_j)\mathbf{D}_2(\omega) + \alpha_4(d_j)\mathbf{O}_2 \quad (9.33)$$

$$\mathbf{D}_{\text{eff}}(d_j, \omega) = \beta_1(d_j)\mathbf{D}_1(\omega) + \beta_2(d_j)\mathbf{O}_1 + \beta_3(d_j)\mathbf{D}_2(\omega) + \beta_4(d_j)\mathbf{O}_2 \quad (9.34)$$

where the coefficients $\alpha_i$ and $\beta_i$ depend on both wavelengths, through the extinction coefficients and also through the ratio of partial to total mean optical pathlengths $\left(\frac{\langle l_i(d_j,\lambda)\rangle}{\langle L(d_j,\lambda)\rangle}\right)$ [30]. The coefficients $\alpha_1$, $\alpha_3$ (in (9.33) for oxy-hemoglobin) and $\beta_2$, $\beta_4$ (in (9.34) for deoxy-hemoglobin) are called cross talk coefficients, and are much smaller than the other coefficients, and usually could be omitted without significantly affecting the results. However, in this study we used (9.33) and (9.34) with no approximations.

We observe that knowledge of the baseline values of the optical properties in the two layers and the thickness of the first layer allows us to calculate all of the coefficients α and β in (9.33) and (9.34). In this work, the shortest source-detector separation was $d_1 = 8$ mm. Considering that the combined scalp and skull thickness in adult human is typically 8–16 mm, we made the reasonable assumption that $\mathbf{O}_{\text{eff}}(d_1, \omega) = \mathbf{O}_1(\omega)$ and $\mathbf{D}_{\text{eff}}(d_1, \omega) = \mathbf{D}_1(\omega)$; in other words, the oxy- and deoxy-hemoglobin phasors obtained with the mBLL from the measured optical signals at the shortest source-detector separation are taken to coincide with the oxy- and deoxyhemoglobin phasors of the top layer. Then, we used (9.33) and (9.34) to retrieve the phasors of oxy- and deoxy-hemoglobin concentrations in the bottom layer, $\mathbf{O}_2(\omega)$ and $\mathbf{D}_2(\omega)$, by using the oxy- and deoxy-hemoglobin phasors obtained with the mBLL from the measured optical signals at the longest source-detector separation, $\mathbf{O}_{\text{eff}}(d_6, \omega)$ and $\mathbf{D}_{\text{eff}}(d_6, \omega)$. The reason for using the longest source-detector distance is that, at this distance, the measured optical intensities are most sensitive to the bottom, cerebral tissue layer.

## 9.4 Experimental Methods

A commercial frequency-domain tissue spectrometer (OxiplexTS, ISS Inc., Champaign, IL) was used in the NIRS measurements that were performed. A frequency of 110 MHz was used for modulating the laser intensity outputs. An optical probe was connected to the spectrometer through optical fibers distributing 690 and 830 nm wavelength light at six different locations, separated 8, 13, 18, 28, 33, and 38 mm from a single collection optical fiber. The optical probe was positioned against the subject's forehead right side and fixed with a flexible headband. The instrument was calibrated through an optical phantom of known optical properties, by means of the so called multidistance FD NIRS procedure [41].

Pneumatic thigh cuffs were swaddled around the person's thighs and plugged to an automated cuff inflation system (E-20 Rapid Cuff Inflation System, D. E. Hokanson, Inc., Bellevue, WA). The thigh cuffs air pressure was continuously monitored

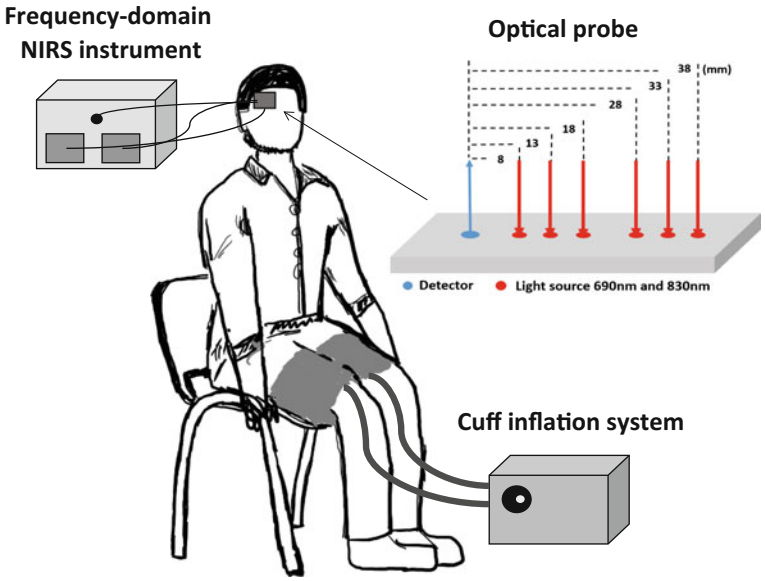


**Fig. 9.3** Schematic of the experimental setup, including the frequency-domain NIRS instrument, the pneumatic thigh cuff, and the automated cuff inflation system. A detail of the optical probe is shown to specify the six source-detector distances used

through a digital manometer (Series 626 Pressure Transmitter, Dwyer Instruments, Inc., Michigan City, IN). The thigh cuff pressure monitor analogue outputs were fed to auxiliary inputs of the NIRS instrument for concomitant recordings together with the NIRS data. A 25 year old healthy female was subjected to an eight cycles protocol, where in each cycle the thigh cuff was inflated to a pressure of 190 mmHg for 9 s and released for 8 s ($f = 0.059$ Hz, where $f = \omega/2\pi$ is the frequency of the cuff inflation/deflation cycles).

The analytic signal method [42, 43] was used to associate phasors (i.e. an amplitude and phase) to the oscillations of oxy- and deoxy-hemoglobin concentrations, which were obtained by using the mBLL as explained in Sect. 9.3.2 ((9.31) and (9.32)). The overall experimental setup layout is displayed in Fig. 9.3.

## 9.5 Results

The frequency-domain multi-distance NIRS data collected in vivo, analyzed with the two-layer diffusion model of Sect. 9.3.1, yielded the values of the baseline optical properties of the two tissue layers and of the thickness of the top layer that are reported in Table 9.1. On the basis of these baseline optical properties and thickness of top layer, we have computed the $\alpha$ and $\beta$ coefficients in the system of (9.33) and (9.34),

**Table 9.1** Baseline optical properties and top layer thickness obtained on the head of a human subject with multi-distance FD NIRS data and a two-layer diffusion model

| | | $\lambda_1$ (690 nm) | $\lambda_2$ (830 nm) |
|---|---|---|---|
| Top layer | $\mu_{a1}$ ($cm^{-1}$) | 0.072 | 0.068 |
| | $\mu_{s1}'$ ($cm^{-1}$) | 12.4 | 12.5 |
| | Thickness (mm) | 9 | |
| Bottom layer | $\mu_{a2}$ ($cm^{-1}$) | 0.089 | 0.10 |
| | $\mu_{s2}'$ ($cm^{-1}$) | 2.7 | 2.1 |

**Table 9.2** Coefficients of the linear combinations of the oxy- and deoxy-hemoglobin concentration phasors in the top and bottom tissue layer ($\mathbf{O}_1$, $\mathbf{D}_1$, $\mathbf{O}_2$, $\mathbf{D}_2$) that result in the effective phasors obtained from CW NIRS data at source-detector separation $d_6 = 38$ mm with the modified Beer-Lambert law ($\mathbf{O}_{\text{eff}}(d_6)$, $\mathbf{D}_{\text{eff}}(d_6)$) (see (9.33) and (9.34))

| | |
|---|---|
| $\alpha_1(d_6)$ | 0.062 |
| $\alpha_2(d_6)$ | 0.63 |
| $\alpha_3(d_6)$ | −0.062 |
| $\alpha_4(d_6)$ | 0.37 |
| $\beta_1(d_6)$ | 0.54 |
| $\beta_2(d_6)$ | −0.016 |
| $\beta_3(d_6)$ | 0.46 |
| $\beta_4(d_6)$ | 0.016 |

for the greater source-detector distance ($d_6 = 38$ mm), as reported in Table 9.2. This is the first step of our hybrid approach: the determination of the coefficients of the linear system of (9.33) and (9.34) that allows us to translate single-distance, CW NIRS measurements of effective oxy- and deoxy-hemoglobin concentration phasors at short distance ($\mathbf{O}_{\text{eff}}$, $\mathbf{D}_{\text{eff}}$ at $d_1 = 8$ mm) and long distance ($\mathbf{O}_{\text{eff}}$, $\mathbf{D}_{\text{eff}}$ at $d_6 = 38$ mm) into the actual hemoglobin concentration phasors in the top layer ($\mathbf{O}_1$, $\mathbf{D}_1$) and bottom layer ($\mathbf{O}_2$, $\mathbf{D}_2$) of the investigated tissue.

Figure 9.4 shows the phasors of the concentrations of oxy- and deoxy-hemoglobin at six source-detector separations derived with the mBLL (top phasors in Fig. 9.4). Even though we have used only the effective phasors measured at the first and the sixth source-detector distances for our method of recovering $\mathbf{O}_2(\omega)$ and $\mathbf{D}_2(\omega)$, in Fig. 9.4 we also show the other effective phasors to illustrate that both oxy- and deoxy-hemoglobin effective phasors rotate clockwise as they are measured farther and farther from the detector. Because larger source-detector separations feature enhanced sensitivities to deeper tissues, this trend is indicative of different oscillations occurring in the extracerebral tissue and in the brain. Specifically, these results indicate that hemodynamic oscillations in the bottom layer have a lower phase than those in the top layer. In other words, deeper hemodynamic oscillations lag superficial hemodynamic oscillations.

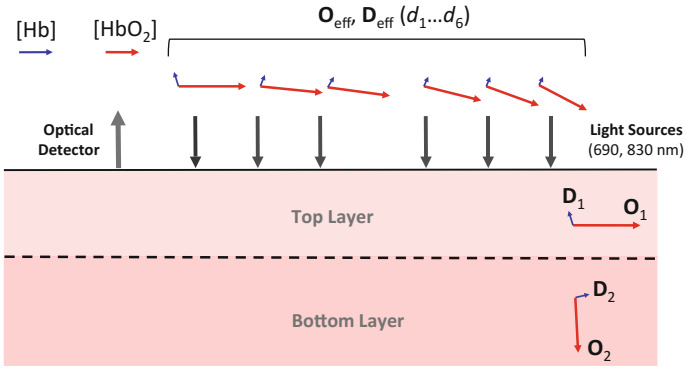


**Fig. 9.4** Schematic illustration of the two-layer tissue model and the set of illumination and collection optical fibers at six source-detector distances (8, 13, 18, 28, 33, and 38 mm). The set of phasors above each illumination optical fiber are the effective oxy- and deoxy-hemoglobin concentration phasors obtained from single-distance CW NIRS data analyzed with the modified Beer-Lambert law. The phasors inside the top and bottom layers represent the actual hemodynamic oscillations in the two layers, as obtained by our hybrid FD/CW NIRS approach

The phases of all phasors were taken relative to the phase of $\mathbf{O}_{\text{eff}}(d_1, \omega) = \mathbf{O}_1(\omega)$ (we recall that the oxy-hemoglobin phasor obtained with the mBLL from the optical data at the shortest source-detector distance, $d_1$, was taken to coincide with the oxy-hemoglobin phasor of the top layer), so that, by definition, Arg $(\mathbf{O}_1(\omega)) = 0°$. With this convention, the effective oxy- and deoxy-hemoglobin phasors obtained from CW NIRS data and the mBLL at the shortest $(d_1)$ and longest $(d_6)$ source-detector distances were: $\mathbf{O}_{\text{eff}}(d_1) = 0.67\,\mu\text{M}\angle 0°$; $\mathbf{D}_{\text{eff}}(d_1) = 0.096\,\mu\text{M}\angle 103°$; $\mathbf{O}_{\text{eff}}(d_6) = 0.49\,\mu\text{M}\angle -28°$; $\mathbf{D}_{\text{eff}}(d_6) = 0.067\,\mu\text{M}\angle 55°$.

As described in Sect. 9.3.2, we identified $\mathbf{O}_{\text{eff}}(d_1)$ and $\mathbf{D}_{\text{eff}}(d_1)$ with the oxy- and deoxy-hemoglobin concentration phasors in the top layer: $\mathbf{O}_1 = 0.67\,\mu\text{M}\angle 0°$ and $\mathbf{D}_1 = 0.096\,\mu\text{M}\angle 103°$. From (9.33) and (9.34), using the coefficients of Table 9.2, we obtained the oxy- and deoxy-hemoglobin concentration phasors in the bottom layer: $\mathbf{O}_2 = 0.62\,\mu\text{M}\angle -87°$ and $\mathbf{D}_2 = 0.11\,\mu\text{M}\angle 13°$. These phasor results for the top and bottom tissue layers, which reflect hemodynamic oscillations at the induced frequency of 0.059 Hz, confirm the qualitative observation that hemodynamic oscillations in the bottom layer lag those in the top layer (in this case, by about 90°).

## 9.6 Discussion and Conclusions

We have described a novel technique, CHS, to perform quantitative studies of cerebral hemodynamics on the basis of data collected with NIRS or fMRI. This technique is combined with a dedicated analytical model that describes arbitrary time courses of oxy- and deoxy-hemoglobin concentrations in tissue (time-domain representation),

or oscillatory hemodynamics at well-defined frequencies (frequency-domain representation). This analytical model enables the translation of measurable hemoglobin concentrations in tissue into physiological quantities of interest for diagnostic assessment, functional studies, or characterization of tissue perfusion. The dynamic study of blood perfusion and oxygenation has been performed for many years using both NIRS and fMRI in a number of research areas. For example, spontaneous low-frequency hemodynamic oscillations have been investigated in studies of resting state functional connectivity based on fMRI [44–46] or NIRS [47–50]. Even more closely related to CHS, several NIRS studies have investigated the relative phase of cerebral [Hb] and [$HbO_2$] oscillations occurring spontaneously [51] or in response to paced breathing [32, 52, 53]. The innovative aspects of CHS are the systematic nature of the measurements of coherent hemodynamics, and the quantitative analysis afforded by the analytical mathematical model.

In the case of non-invasive NIRS studies of the human brain, one has to take into consideration the presence of superficial, non-cerebral tissue layers that may confound optical measurements of the brain cortex. This is a well-known limiting factor of non-invasive functional NIRS, which has been tackled in a number of ways, typically based on collecting data at multiple source-detector separations in combination with regression methods [26], spectral analysis [54], independent component analysis [55], or the computation of partial mean pathlengths in two-layered media [56].

This chapter describes a hybrid FD/CW method based on the mBLL and on a two-layer diffusion model to disentangle the contributions to the optical signals from induced hemodynamic oscillations occurring in the extracerebral (superficial) tissue and in the (deeper) brain tissue. This problem was tackled by using a two-layer diffusion model and the combination of NIRS data collected at multiple source-detector separations. This two-layer diffusion model has by now been used in the evaluation of baseline optical features and hemoglobin concentrations in two "effective" head tissue layers. Frequently, in NIRS, the dynamics of hemoglobin species are calculated by means of the modified Beer-Lambert law (mBLL), which considers homogeneous absorption changes in a light probed tissue. As this premise can be violated under a variety of conditions, it would be fundamental to distinguish the hemodynamic oscillations taking place in the extra-cerebral layers, namely scalp and skull, from those taking place in the brain. Thereupon a more realistic two distinct layers model of the head has been considered. The diffusion equation solution in the FD corresponding to a two-layer configuration was used to recover the absorption baseline values, the reduced scattering coefficients of both layers, and also the first layer thickness, from frequency-domain data at six source-detector separations. These baseline values were used to calculate the partial (in each layer) and total (in the entire medium) mean optical pathlengths which allowed us to recover the oxy- and deoxy-hemoglobin hemodynamic oscillations in the two tissue layers by using CW data. This is the first step to recover relevant physiological parameters specific to the brain by using CHS.

In summary, we have described CHS, a new technique to investigate cerebral hemodynamics, and a first attempt towards the creation of depth-resolved CHS.

The ability to perform accurate measurements of the cerebral hemodynamics with non-invasive optical techniques can ultimately result in a powerful tool towards the non-invasive assessment of cerebral perfusion, autoregulation, functional activation, and overall tissue viability in vivo.

**Acknowledgements** This research is supported by the US National Institutes of Health (Grants no. R01-NS095334 and R21-EB020347).

## References

1. R.B. Buxton, L.R. Frank, A model of the coupling between cerebral blood flow and oxygen metabolism during neural stimulation. J. Cereb. Blood Flow Metab. **17**, 64–72 (1997)
2. J.B. Mandeville, J.J.A. Marota, C. Ayata, G. Zaharchuk, M.A. Moskowitz, B.R. Rosen, R.M. Weisskoff, Evidence of a cerebrovascular postarteriole windkessel with delayed compliance. J. Cereb. Blood Flow Metab. **19**, 679–689 (1999)
3. M. Ferrari, V. Quaresima, A brief review on the history of human functional near-infrared spectroscopy (fNIRS) development and fields of application. NeuroImage **63**, 921–935 (2012)
4. F. Scholkmann, S. Kleiser, A.J. Metz, R. Zimmermann, J.M. Pavia, U. Wolf, M. Wolf, A review on continuous wave functional near-infrared spectroscopy and imaging instrumentation and methodology. NeuroImage **85**, 6–27 (2014)
5. A. Torricelli, D. Contini, A. Pifferi, M. Caffini, R. Re, L. Zucchelli, L. Spinelli, Time domain functional NIRS imaging for human brain mapping. NeuroImage **85**, 28–50 (2014)
6. M. Smith, Shedding light on the adult brain: a review of the clinical applications of near-infrared spectroscopy. Philos. Trans. R. Soc. A **369**, 4452–4469 (2011)
7. A. Casati, G. Fanelli, P. Pietropaoli, R. Tufano, G. Danelli, G. Fierro, G. De Cosmo, G. Servillo, Continuous monitoring of cerebral oxygen saturation in elderly patients undergoing major abdominal surgery minimizes brain exposure to potential hypoxia. Anesth. Analg. **101**, 740–747 (2005)
8. M.M. Tisdall, I. Tachtsidis, T.S. Leung, C.E. Elwell, M. Smith, Increase in cerebral aerobic metabolism by normobaric hyperoxia after traumatic brain injury. J. Neurosurg. **109**, 424–432 (2008)
9. S.R. Leal-Noval, A. Cayuela, V. Arellano-Orden, A. Marin-Caraballos, V. Padilla, C. Ferrándiz-Millón, Y. Corcia, C. García-Alfaro, R. Amaya-Villar, F. Murillo-Cabezas, Invasive and noninvasive assessment of cerebral oxygenation in patients with severe traumatic brain injury. Intens. Care Med. **36**, 1309–1317 (2010)
10. F. Fabbri, M.E. Henry, P.F. Renshaw, S. Nadgir, B.L. Ehrenberg, M.A. Franceschini, S. Fantini, Bilateral near-infrared monitoring of the cerebral concentration and oxygen saturation of hemoglobin during right unilateral electro-convulsive therapy. Brain Res. **992**, 193–204 (2003)
11. V. Toronov, A. Webb, J.H. Choi, M. Wolf, L. Safonova, U. Wolf, E. Gratton, Study of local cerebral hemodynamics by frequency-domain near-infrared spectroscopy and correlation with simultaneously acquired functional magnetic resonance imaging. Opt. Express **9**, 417–427 (2001)
12. A.M. Siegel, J.P. Culver, J.B. Mandeville, D.A. Boas, Temporal comparison of functional brain imaging with diffuse optical tomography and fMRI during rat forepaw stimulation. Phys. Med. Biol. **48**, 1391–1403 (2003)
13. A. Sassaroli, B. deB. Frederick, Y. Tong, P.F. Renshaw, S. Fantini, Spatially weighted BOLD signal for comparison of functional magnetic resonance imaging and near-infrared imaging of the brain. NeuroImage **33**, 505–514 (2006)
14. X. Cui, S. Bray, D.M. Bryant, G.H. Glover, A.L. Reiss, A quantitative comparison of NIRS and fMRI across multiple cognitive tasks. NeuroImage **54**, 2808–2821 (2011)

15. T.J. Huppert, M.S. Allen, H. Benav, P.B. Jones, D.A. Boas, A multicompartment vascular model for inferring baseline and functional changes in cerebral oxygen metabolism and arterial dilation. J. Cereb. Blood Flow Metab. **27**, 1262–1279 (2007)
16. M. Banaji, A. Mallet, C.E. Elwell, P. Nicholls, C.E. Cooper, A model of brain circulation and metabolism: NIRS signal changes during physiological challenges. PLoS Comput. Biol. **4**, e1000212 (2008)
17. D.A. Boas, S.R. Jones, A. Devor, T.J. Huppert, A.M. Dale, A vascular anatomical network model of the spatio-temporal response to brain activation. NeuroImage **40**, 1116–1129 (2008)
18. S.G. Diamond, K.L. Perdue, D.A. Boas, A cerebrovascular response model for functional neuroimaging including cerebral autoregulation. Math. Biosci. **220**, 102–117 (2009)
19. S. Fantini, Dynamic model for the tissue concentration and oxygen saturation of hemoglobin in relation to blood volume, flow velocity, and oxygen consumption: implications for functional neuroimaging and coherent hemodynamics spectroscopy (CHS). NeuroImage **85**, 202–221 (2014)
20. S. Fantini, A new hemodynamic model shows that temporal perturbations of cerebral blood flow and metabolic rate of oxygen cannot be measured individually using functional near-infrared spectroscopy. Physiol. Meas. **35**, N1–N9 (2014)
21. D.T. Delpy, M. Cope, P. van der Zee, S. Arridge, S. Wray, J. Wyatt, Estimation of optical path length through tissue from direct time of flight measurements. Phys. Med. Biol. **33**, 1433–1442 (1988)
22. A. Sassaroli, S. Fantini, Comment on the modified Beer-Lambert law for scattering media. Phys. Med. Biol. **49**, N1–N3 (2004)
23. J. Choi, M. Wolf, V. Toronov, U. Wolf, C. Polzonetti, D. Hueber, L.P. Safonova, R. Gupta, A. Michalos, W. Mantulin, E. Gratton, Noninvasive determination of the optical properties of adult brain: near-infrared spectroscopy approach. J. Biomed. Opt. **9**, 221–229 (2004)
24. L. Gagnon, C. Gauthier, R.D. Hoge, F. Lesage, J. Selb, D.A. Boas, Double-layer estimation of intra- and extracerebral hemoglobin concentration with a time-resolved system. J. Biomed. Opt. **13**, 054019 (2008)
25. B. Hallacoglu, A. Sassaroli, S. Fantini, Optical characterization of two-layered turbid media for non-invasive, absolute oximetry in cerebral and extracerebral tissue. PLoS ONE **8**, e64095 (2013)
26. R.B. Saager, A.J. Berger, Direct characterization and removal of interfering absorption trends in two-layer turbid media. J. Opt. Soc. Am. A **22**, 1874–1882 (2005)
27. Q. Zhang, G.E. Strangman, G. Ganis, Adaptive filtering to reduce global interference in non-invasive NIRS measures of brain activation: how well and when does it work? NeuroImage **45**, 788–794 (2009)
28. L. Gagnon, K. Perdue, D.N. Greve, D. Goldenholz, G. Kaskhedikar, D.A. Boas, Improved recovery of the hemodynamic response in diffuse optical imaging using short optode separations and state-space modeling. NeuroImage **56**, 1362–1371 (2011)
29. F. Scarpa, S. Brigadoi, S. Cutini, P. Scatturin, M. Zorzi, R. Dell'Acqua, G. Sparacino, A reference-channel based methodology to improve estimation of event-related hemodynamic response from fNIRS measurements. NeuroImage **72**, 106–119 (2013)
30. F. Zheng, A. Sassaroli, S. Fantini, Phasor representation of oxy- and deoxyhemoglobin concentrations: what is the meaning of out-of-phase oscillations as measured by near-infrared spectroscopy? J. Biomed. Opt. **15**, 040512 (2010)
31. J.M. Kainerstorfer, A. Sassaroli, S. Fantini, Optical oximetry of volume-oscillating vascular compartments: contributions from oscillatory blood flow. J. Biomed. Opt. **21**, 101408 (2016)
32. M. Reinhard, E. Wehrle-Wieland, D. Grabiak, M. Roth, B. Guschlbauer, J. Timmer, C. Weiller, A. Hetzel, Oscillatory cerebral hemodynamics: the macro- vs. microvascular level. J. Neurol. Sci. **250**, 103–109 (2006)
33. M.L. Pierro, J.M. Kainerstorfer, A. Civiletto, D.E. Wiener, A. Sassaroli, B. Hallacoglu, S. Fantini, Reduced speed of microvascular blood flow in hemodialysis patients versus healthy controls: a coherent hemodynamics spectroscopy study. J. Biomed. Opt. **19**, 026005 (2014)

34. J.M. Kainerstorfer, A. Sassaroli, K.T. Tgavalekos, S. Fantini, Cerebral autoregulation in the microvasculature measured with near-infrared spectroscopy. J. Cereb. Blood Flow Metab. **35**, 959–966 (2015)
35. S. Fantini, A. Sassaroli, J.M. Kainerstorfer, K.T. Tgavalekos, X. Zang, Non-invasive assessment of cerebral microcirculation with diffuse optics and coherent hemodynamics spectroscopy. Proc. SPIE **9690**, 96900S (2016)
36. G. Alexandrakis, D.R. Busch, G.W. Faris, M.S. Patterson, Determination of the optical properties of two-layer turbid media by use of a frequency-domain hybrid Monte Carlo diffusion model. Appl. Opt. **40**, 3810–3821 (2001)
37. T.H. Pham, T. Spott, L.O. Svaasand, B.J. Tromberg, Quantifying the properties of two layer turbid media with frequency-domain diffuse reflectance. Appl. Opt. **39**, 4733–4745 (2000)
38. F. Martelli, A. Sassaroli, S. Del Bianco, Y. Yamada, G. Zaccanti, Solution of the time-dependent diffusion equation for layered diffusive media by the eigenfunction method. Phys. Rev. E **67**, 056623 (2003)
39. J. Ripoll, V. Ntziachristos, J.P. Culver, D.N. Pattanayak, A.G. Yodh, M. Nieto-Vesperinas, Recovery of optical parameters in multiple-layered diffusive media: theory and experiments. J. Opt. Soc. Am. A **18**, 821–830 (2001)
40. A. Liemert, A. Kienle, Light diffusion in N-layered turbid media: frequency and time domains. J. Biomed. Opt. **15**, 025002 (2010)
41. S. Fantini, M.A. Franceschini, E. Gratton, Semi-infinite-geometry boundary problem for light migration in highly scattering media: a frequency-domain study in the diffusion approximation. J. Opt. Soc. Am. B **11**, 2128–2138 (1994)
42. B. Boashash, Estimating and interpreting the instantaneous frequency of a signal. Part 1: Fundamentals. Proc. IEEE **80**, 520–538 (1992)
43. M. Pierro, A. Sassaroli, P.R. Bergethon, B.L. Ehrenberg, S. Fantini, Phase-amplitude investigation of spontaneous low-frequency oscillations of cerebral hemodynamics with near-infrared spectroscopy: a sleep study in human subjects. NeuroImage **63**, 1571–1584 (2012)
44. B.B. Biswal, F.Z. Yetkin, V.M. Haughton, J.S. Hyde, Functional connectivity in the motor cortex of resting human brain using echo-planar MRI. Magn. Reson. Med. **34**, 537–541 (1995)
45. M.D. Greicius, B. Krasnow, A.L. Reiss, V. Menon, Functional connectivity in the resting brain: a network analysis of the default mode hypothesis. Proc. Nat. Acad. Sci. USA **100**, 253–258 (2003)
46. M.D. Fox, M.E. Raichle, Spontaneous fluctuations in brain activity observed with functional magnetic resonance imaging. Nature **8**, 700–711 (2007)
47. B.R. White, A.Z. Snyder, A.L. Cohen, S.E. Petersen, M.E. Raichle, B.L. Schlaggar, J.P. Culver, Resting-state functional connectivity in the human brain revealed with diffuse optical tomography. NeuroImage **47**, 148–156 (2009)
48. C.M. Lu, Y.J. Zhang, B.B. Biswal, Y.F. Zang, D.L. Peng, C.Z. Zhu, Use of fNIRS to assess resting state functional connectivity. J. Neurosci. Methods **186**, 242–249 (2010)
49. S. Sasai, H. Fumitaka, H. Watanabe, G. Taga, Frequency-specific functional connectivity in the brain during resting state revealed by NIRS. NeuroImage **56**, 252–257 (2011)
50. A. Sassaroli, M. Pierro, P.R. Bergethon, S. Fantini, Low-frequency spontaneous oscillations of cerebral hemodynamics investigated with near-infrared spectroscopy: a review. IEEE J. Sel. Top. Quantum Electron. **18**, 1478–1492 (2012)
51. G. Taga, Y. Konishi, A. Maki, T. Tachibana, M. Fujiwara, H. Koizumi, Spontaneous Oscillation of oxy- and deoxy-hemoglobin changes with a phase difference throughout the occipital cortex of newborn infants observed using non-invasive optical topography. Neurosci. Lett. **282**, 101–104 (2000)
52. H. Obrig, M. Neufang, R. Wenzel, M. Kohl, J. Steinbrink, K. Einhäupl, A. Villringer, Spontaneous low frequency oscillations of cerebral hemodynamics and metabolism in human adults. NeuroImage **12**, 623–639 (2000)
53. F. Tian, H. Niu, B. Khan, G. Alexandrakis, K. Behbehani, H. Liu, Enhanced functional brain imaging by using adaptive filtering and a depth compensation algorithm in diffuse optical tomography. IEEE Trans. Med. Imag. **30**, 1239–1251 (2011)

54. O. Pucci, V. Toronov, K. St.Lawrence, Measurement of the optical properties of a two-layer model of the human head using broadband near-infrared spectroscopy. Appl. Opt. **49**, 6324–6332 (2010)
55. T. Funane, H. Atsumori, T. Katura, A.N. Obata, H. Sato, Y. Tanikawa, E. Okada, M. Kiguchi, Quantitative evaluation of deep and shallow tissue layers' contribution to fNIRS signal using multi-distance optodes and independent component analysis. NeuroImage **85**, 150–165 (2014)
56. L. Zucchelli, D. Contini, R. Re, A. Torricelli, L. Spinelli, Method for the discrimination of superficial and deep absorption variations by time domain fNIRS. Biomed. Opt. Express **4**, 2893–2910 (2013)